Title

Walk-Burrow-Tug: Legged Anchoring Analysis Using RFT-Based Granular Limit Surfaces

Journal

IEEE Robotics and Automation Letters, 8(6)

ISSN

2377-3766

Authors

Huh, Tae Myung
Cao, Cyndia
Aderibigbe, Jadesola
et al.

Publication Date

2023

DOI

10.1109/lra.2023.3269324

Walk-Burrow-Tug: Legged Anchoring Analysis Using RFT-Based Granular Limit Surfaces

Tae Myung Huh, *Member, IEEE*, Cyndia Cao, *Graduate Student Member, IEEE*, Jadesola Aderibigbe, Deaho Moon, and Hannah S. Stuart, *Senior Member, IEEE*

***Abstract*—We develop a new resistive force theory based granular limit surface (RFT-GLS) method to predict and guide behaviors of forceful ground robots. As a case study, we harness a small mobile robotic system – MiniRQuad (296 g) – to 'walk-burrow-tug;' it actively exploits ground anchoring by burrowing its legs to tug loads. RFT-GLS informs the selection of efficient strategies to transport sleds with varying masses. The granular limit surface (GLS), a wrench boundary that separates stationary and kinetic behavior, is computed using 3D resistive force theory (RFT) for a given body and set of motion twists. This limit surface is then used to predict the quasi-static trajectory of the robot when it fails to withstand an external load. We find that the RFT-GLS enables accurate force and motion predictions in laboratory tests. For control applications, a pre-composed state space map of the twist-wrench pairs enables computationally efficient simulations to improve robotic anchoring strategies.**

***Index Terms*—Contact modeling, legged robots, mobile manipulation, granular limit surface.**

I. Introduction

ROBOTIC systems demonstrate impressive mobility in granular media, even in loose sand with low traction as summarized in [1], [2], [3]. Anchoring, or resisting forces while statically planted in or on media, is relatively less studied for robotic systems in granular terrain as compared with mobility. Fernandez and Mazumdar (2021) [4] present a wheeled vehicle with a hammer-like tail to engage with sandy surfaces that can resist tugging loads up to about 6 times its mass. Creager et al. (2015) demonstrate a lunar rover that uses wheel anchoring for mobility in extremely loose media [5]. Another strategy is to anchor through burrowing. As described in the review article by Wei et al. (2021) [6], there exist several burrowing robots inspired by arthropods [7], [8], clams [9], [10], worms [11], and plant roots [12], [13]; only [13] notes anchoring capabilities. Beyond granular media applications, anchors enable new mobility and manipulation capabilities. For example, a milli-robot with gecko-inspired adhesives can adhere to a smooth, flat surface to perform forceful tugging manipulations [14], [15]. On rough or rocky surfaces, robotic limbs with micro-spines grab onto asperities, allowing small aerial robots to achieve high holding force [15] or stable climbing maneuvers [16]. This letter presents a legged robot simply anchoring in a granular media by burrowing its C-shaped legs without any additional hardware. We developed the granular anchor analysis tool (RFT-GLS) that (1) estimates the limit of the resistible force and moment of a given anchor pose and (2) predicts the quasi-static motion of a slipping anchor. Using this tool, as depicted in Fig. 1, our legged platform tugs a payload across loose sand by setting leg anchors in a pose that sufficiently resists the tugging force.

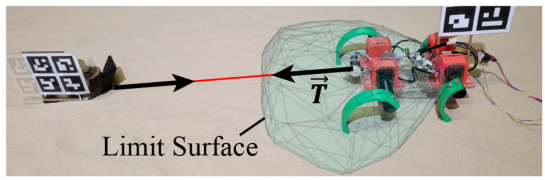

Fig. 1. Example of limit surface application in the granular media. Our "MiniRQuad," modified into a quadruped robot from MiniRHex [17], needs to winch a load so it partially buries its legs to increase its load capacity. If the pull force ($\vec{T}$) is inside the limit surface, the anchored MiniRQuad will winch the load without slipping.

A. Modeling Granular Interactions

Granular Resistive Force Theory (RFT) is an empirical method to model the interactions between robotic systems and granular media. As a closed-form calculation, it is especially useful for rapid parametric studies and control analyses. Prior applications of RFT include legged running [18], [19], a bioinspired snake-like robot [19], compliant fins for near-surface locomotion [20], rover wheels in highly dynamic motions [21], [22], mole-crab inspired burrowing [8], and differential speed driving control of rovers [23]; these analyses exclude static anchoring. Granular RFT computes forces with respect to the velocity direction and thus is not valid when speed is zero when a body is anchored.

Other geotechnical analyses of ground anchors exist using the weight of the media and the shear and normal stresses at the failure surface [24], [25], cavity expansion theory [26], upper-/lower-limit analysis [27], and reverse hopper theory [28];

Manuscript received 12 December 2022; accepted 5 April 2023. Date of publication 21 April 2023; date of current version 11 May 2023. This letter was recommended for publication by Associate Editor M. Costanzo and Editor H. Liu upon evaluation of the reviewers' comments. This work was supported in part by an Early Career Faculty under Grant 80NSSC21K0069 and in part by the Space Technology Research Fellowship under Grant 80NSSC19K1167 through NASA's Space Technology Research Grants Program. *(Corresponding author: Tae Myung Huh.)*

Tae Myung Huh is with the Baskin School of Engineering, Department of Electrical and Computer Engineering, Univeristy of California at Santa Cruz, Santa Cruz, CA 95064 USA (e-mail: thuh@ucsc.edu).

Cyndia Cao, Jadesola Aderibigbe, Deaho Moon, and Hannah S. Stuart are with the School of Engineering, Department of Mechanical Engineering, University of California at Berkeley, Berkeley, CA 94709 USA (e-mail: cyndia_cao@berkeley.edu; jadesola@berkeley.edu; dmoon0322@kist.re.kr; hstuart@berkeley.edu).

This letter has supplementary downloadable material available at https://doi.org/10.1109/LRA.2023.3269324, provided by the authors.

Digital Object Identifier 10.1109/LRA.2023.3269324

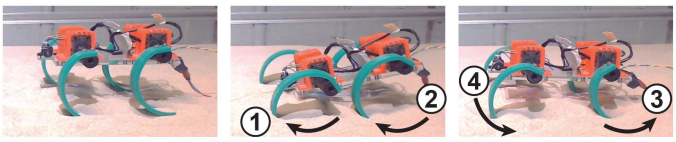

(a) Standing (b) Retracting (c) Final

Fig. 2. MiniRQuad burrows the legs to increase its tugging load capacity. Here is one example sequence for burrowing the legs starting from standing.

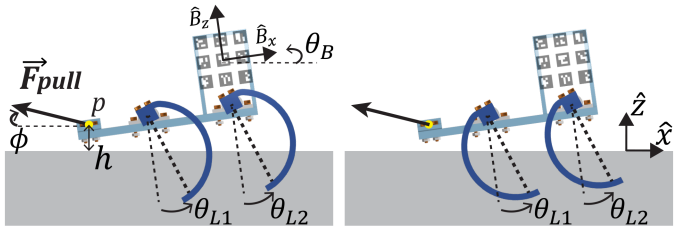

(a) Forward Pull (b) Backward Pull

Fig. 3. Quadruped robot test setup. (a) Forward and (b) backward pulls are tested by switching the leg orientations. The forward direction is defined as the MiniRhex forward walking direction.

an overview of other approaches are described in [29]. Numerical approaches, i.e. Finite Element Method (FEM) [27], [30], [31] and Discrete Element Method (DEM) [32], [33], simulate the behavior of the grains surrounding the anchor for accurate load capacity estimates. Most non-numerical methods do not predict motion and assume simple flat geometries (e.g., disk, strip, pipe) and simple load cases (e.g. pulling perpendicular to the anchor's surface). While numerical methods avoid these simplifications, heavy computational loads, i.e. hours or days of computation, are a barrier to rapid parametric analyses. There remains a need for fast, i.e. in a matter of seconds, and generalizable static and quasi-static methods to analyze forceful tugging robot behaviors in granular media. Limit surfaces – a boundary in wrench space which contains the forces and torques acting on the body separating non-slip (stationary) states and slip states [34], [35] – are commonly used to efficiently model contact-rich robotic interactions, like dexterous manipulation with soft frictional skin [36], [37]. For robot interactions with granular media, Zhu et al. (2019) developed a machine learning method, which uses training data collected via experiments and DEM simulations to obtain a cylindrical object's limit surface given its positional state [38]. We propose a new method of obtaining granular limit surfaces that relies on the RFT model, rather than time consuming experiments or DEM simulations, that is generalizable to new shapes.

B. Overview

Section II first defines the modeling objectives of the present work. Section III then describes the proposed Resistive Force Theory Granular Limit Surface (RFT-GLS) method. We then describe the methods used to experimentally test the validity of the limit surface to estimate anchor forces and quasi-static motions in Section IV. Results are reported in Section V. In Section VI, we demonstrate an example robotic application, using RFT-GLS to predict and inform the ability of the MiniRQuad to winch different payloads efficiently. Finally, Section VII discusses our findings in the context of future work, highlighting the potential of this formulation to efficiently generalize to other scenarios.

II. Problem Statement

Our goal is to estimate the maximum tugging force of a RHex-type robot that anchors its legs in the granular media. We also aim to predict the motion trajectory of the legged robot when anchoring fails due to excessive tugging forces. The C-shaped legs of the MiniRQuad can embed in granular media using the open-loop burrowing gait depicted in Fig. 2. By estimating the load capacity of the resulting depth and pose of the legs, the robot can evaluate whether it has sufficient support to tug the target load. In the case of anchor movement, the robot can evaluate whether the predicted motion is detrimental or beneficial to tugging capacity.

A. System

To demonstrate our methodology, we employ a small legged robot equipped with a winch, which can be attached on either the front or back of the robot, as shown in Fig. 3 parts (a) and (b) respectively. The 2D tug load is applied in the sagittal ($\hat{B}_x$-$\hat{B}_z$) plane of the robot. The legged robot is simplified to a quadruped and the leg angles are symmetric about the sagittal plane, reducing the dimension of the configuration space in this study. Only the legs are in contact with a homogeneous and loosely packed granular media. While tugging, the leg angles are fixed with respect to the robot body frame (B). When the leg anchor fails (i.e. moves), the robot motion is assumed to be quasi-static. We assume the load is pulled at a fixed angle ϕ applied by the winch at point p.

B. Objectives

The first objective is to formulate the function ($\mathcal{F}$) that estimates the tugging load capacity ($\overrightarrow{F}_{pull,\max}$):

$$\mathcal{F}(h, \theta_B, \theta_{L1}, \theta_{L2}) = \overrightarrow{F}_{pull,\max} \tag{1}$$

where h is the $\hat{z}$ height of the winch point p, θ_B is the body pitch angle, θ_{L1} and θ_{L2} are the leg angle of each axle defined in robot body frame (B), and $\overrightarrow{F}_{pull,\max}$ is the tugging load capacity.

The second objective is to formulate the function ($\mathcal{G}$) that estimates robot motion with anchor failure:

$$\mathcal{G}(h, \theta_B, \theta_{L1}, \theta_{L2}, \overrightarrow{F}_{pull,\max}) = [v_x, v_z, \omega_y] \tag{2}$$

where v_x, v_z, ω_y are the translational and rotational velocity of the robot in the Newtonian frame. For both objectives, we formulate $\mathcal{F}$ and $\mathcal{G}$ by using RFT-GLS.

III. RFT-GLS Modeling Methods

We first estimate the wrenches and twists – force-moment vectors and translational-angular velocity vectors, respectively – of a buried body using RFT. We use these calculations to generate a GLS, which is then applied to legged tugging.

A. Resistive Force Theory (RFT)

RFT models the force that resists an object's motion in a fluidic media as segment-wise interactions [39]. When each

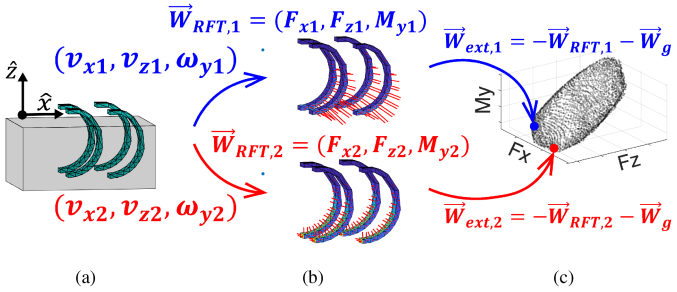

Fig. 4. Procedure to obtain the limit surface of an anchor subject for X-Z planar motions: (a)→(b) compute resistive force (via 3D RFT) experienced during many sampled motion twists to obtain corresponding wrenches; (b)→(c) plot computed wrenches in the wrench space to build a point cloud of the limit surface.

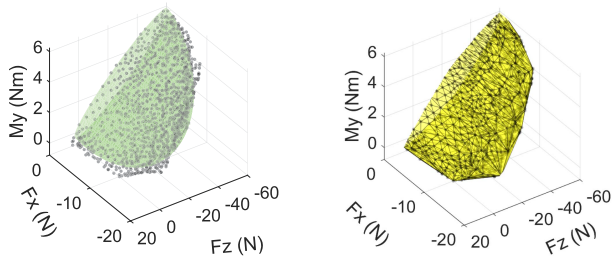

(a) Ellipsoidal fit for Fx < 0 (pull) (b) Alpha-shape boundary for Fx < 0

Fig. 5. Approximated limit surface from the point cloud of sampled RFT twists using (a) ellipsoidal fitting and (b) alpha-shape boundary. Plots show only the small portion of the wrench space representing all upward ($F_z > 0$ N) and light downward forces of magnitude less than 5 N relevant to the present tugging application.

surface segment (ds) of an object in an orientation ($\hat{t}$) moves with a velocity ($\vec{v}$), the overall forces experienced ($\vec{F}$) are integrated as [19]:

$$\vec{F} = \int ds[\, f_{\perp}(\vec{v}, \hat{t})\hat{n} + f_{\parallel}(\vec{v}, \hat{t})\hat{t}\,] \tag{3}$$

where empirical coefficients $f_{\perp}$ and $f_{\parallel}$ depend upon ($\vec{v}, \hat{t}$).

The present work is performed in three-dimensions (3D), leveraging work by Treers et al. (2021) that developed the first 3D granular RFT implementation method [40] as an expansion to [18]; it is applied to mesh representations of a rigid body to estimate resistive force-moment wrenches given its motion twists. We use RFT coefficients obtained and interpolated from penetrometry tests (see supplementary material for coefficients), and specifically do not approximate coefficients from discrete Fourier transformation, as in [18], because such approximations reduce accuracy in the pullout direction. However, the general RFT-GLS framework presented can use any alternative RFT coefficients, as in [41].

RFT assumes that resistive forces are speed-independent at low speeds [18], so the output forces of RFT only depend on the direction of the motion vector. We assume quasi-static motion since, even upon soil failure, the motions tested remain at low speeds with negligible inertial effects [22]. Throughout this work, we also assume that the peak static resistive force and the kinetic resistive force are equal, since sand typically reaches its steady-state, critically packed state after a short displacement, regardless of its initial packing density [42]. These assumptions allow the existing 3D RFT model, which describes forces on moving objects, to also provide wrench information about stationary objects.

B. Granular Limit Surface (GLS) from RFT

We compute the wrench limit surface of the leg anchors with a specified depth and pose, $(h, \theta_B, \theta_{L1}, \theta_{L2})$, following the process in Fig. 4, requiring only the CAD file of the anchor and the RFT coefficients of the granular media. First, the geometry of the robot legs are imported from a CAD file as a surface mesh (Fig. 4(a)). The meshes are placed at a target depth and orientation, while a range of motion twists are simulated to compute their resultant resistive wrenches using 3D RFT (Fig. 4(b)). The reference point of the twist is set on the winch (p). Due to the speed-independence assumption, the limit surface can be sampled via unit twist vectors in various directions. Because loads are constrained to the saggital plane, the resultant wrenches will form a limit surface in a 3D wrench space of (F_x, F_z, M_y) as shown in Fig. 4(c). The limit surface is defined in the wrench space of external inputs ($\vec{W}_{ext}$) that counteract both gravity ($\vec{W}_G$) and granular resistive wrenches ($\vec{W}_{RFT}$) to comply with the quasi-static assumption, such that $\vec{W}_{ext} = -\vec{W}_{RFT} - \vec{W}_G$.

We compare two methods for extrapolating the full limit surface from the sampled twist-wrench pairs (Fig. 4(c)): ellipsoidal approximation and alpha-shape boundaries. Similar to [35], a sampled limit surface can be estimated as an ellipsoidal shape as in Fig. 5(a). The ellipsoidal approximation is formulated by a simple polynomial equation and is selected because it is efficient to use. To minimize the ellipsoidal fit errors, we utilize a fit over the region of interest, i.e. the pullout direction, or $F_x < 0$, as shown. Alternatively, the entire limit surface can be defined by an alpha-shape boundary [43] of the sampled wrenches as in Fig. 5(b). The alpha shape is a polytope that encloses all points and its geometric detail is set by $\alpha \in \mathbb{R}$. We use the *"alphaShape"* featured in MATLAB with the α-radius set by the median of all possible α-radii that generate a unique single domain with a closed boundary. We do not use a convex hull, an infinite α-radius, because it obscures the fine geometric details of the true limit surface. The alpha-shape boundary must store the connectivity of all facets, and is therefore less efficient to use. However it also captures more local details of the limit surface as compared with the ellipsoidal method.

C. Load Capacity Estimation From the GLS

When applied to legged tugging, the moment applied by a string at a winch point must be zero: $\vec{M}_{ext,p} = \vec{0}$. Therefore, the 3D limit surface of the legged robot-winch system is constrained into a limit curve in (F_x, F_z) space. This limit curve is the function $\mathcal{F}$ that maps the legged robot state to $\vec{F}_{pull,\max}$. For an ellipsoidal limit surface approximation, the constrained limit curve is obtained by setting $M_y = 0$ in the polynomial expression, depicted as blue curve in Fig. 6(a). With the alpha-shape boundary method, the limit curve is obtained by the intersection of the alpha-shape boundary and the $M_y = 0$ plane, depicted as blue curve in Fig. 6(b).

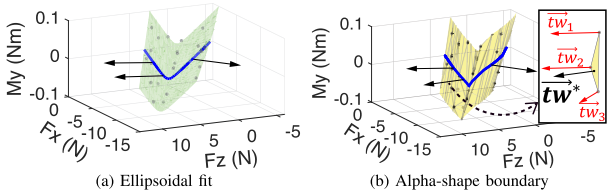

(a) Ellipsoidal fit (b) Alpha-shape boundary

Fig. 6. Estimating the load capacity and twist, $\overrightarrow{\mathbf{tw}}^*$, from the two limit surface fit methods tested in this work.

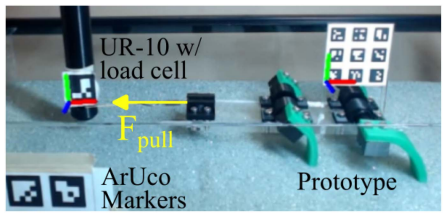

Fig. 7. The experimental test-bed consists of a prototypes mock-up of the quadrupedal robot, which is pulled by a robot arm controlled to maintain a horizontal F_{pull}. Posed are measured with ArUco markers on the arm, prototype and tank.

D. Motion Estimation From the GLS

When the leg anchor fails and the robot starts to slip with quasi-static motions, we assume it will experience the loads on the limit curve. We explore two methods for predicting instantaneous motion of the slipping robot using RFT-GLS.

The first method predicts motions to be aligned with the surface normal of the limit surface. This is inspired by the maximum power dissipation principle for dry contacts [34]. Using this approach for the GLS-ellipsoidal fit, the motion prediction function ($\mathcal{G}$) is a gradient of the ellipsoid expression. Several example twist vectors are shown in Fig. 6(a). This method only considers the power dissipation of the object and ignores the surrounding media [38]. The potential benefit of this simplified method is that it does not require storing the twists that produced the GLS.

The second method interpolates between the wrench vertices of the alpha-shape boundary and their corresponding twists. As described in Section III-B, each wrench on the GLS is produced by a corresponding twist, so the slipping wrench can be correlated to a specific instantaneous motion. The twist of a given wrench on the GLS is obtained by barycentric interpolation [44] of the twists that produce the vertices of the facet in the alpha-shape method ($\overrightarrow{tw}_{1,2,3}$) as shown in Fig. 6(b). Unlike the gradient method, this interpolation method takes into account the movements of adjacent granular media because it is included in the empirical RFT coefficients. Since granular media is not expected to follow the maximum power dissipation principle, interpolated motion estimates (alpha-shaped) are expected to be more accurate than those using the gradient method (ellipsoidal).

E. Pre-Computation of State Space Map for Estimations

For a given arbitrary pose and depth of the legged robot, on-line computation of the load capacity and the failure displacement direction using RFT-GLS is possible but time consuming. Instead, using a sample set of feasible state variables, we generate a load capacity and motion twist map which can be computed prior to robot deployment and used onboard given any arbitrary state by calculating simple and efficient linear interpolations. The state variables of our legged robot prototype are $(h, \theta_B, \theta_{L1}, \theta_{L2})$ as depicted in Fig. 3. The range of state variables are $\theta_{L1,L2} = [-40^\circ, 40^\circ]$ in 20° increments (or $[-40:20:40]^\circ$), $\theta_B = [-20:10:20]^\circ$, and $h = [5:5:30]$ mm. We build state space maps of $\overrightarrow{F}_{pull,\max}$ and $[v_x, v_z, \omega_y]$ by using ellipsoidal approximation and alpha-shape boundary method separately, for comparison with experimental outcomes.

IV. Model Validation Methods

We validate our method to estimate the tugging load capacity ($\mathcal{F}$) and the motion with the failed leg anchor ($\mathcal{G}$) via pull tests on the quadruped prototype pictured in Fig. 7. The quadruped prototype matches the model in Fig. 3 and has four C-shaped legs with a 90 mm diameter and 5 mm thickness. The proximal and distal axles are located at 50 mm and 120 mm from p, respectively. The weight of the fabricated prototype is 120 g. The proximal and distal legs are staggered in the $\hat{B}_y$ direction so that they are unobstructed in the pull direction.

A string is tied to the winch point p and pulled slowly by a robot arm (UR-10); we emulate load conditions which are equivalent to winching by using the arm's load cell (Axia 80, ATI) to maintain horizontal loading, $\phi = 0$. Pull forces are recorded while the motion of the legged robot prototype is measured by tracking ArUco markers. The initial θ_B is set to $0 \pm 4^\circ$ and h is set to 2 cm $\pm$ 5 mm. We test each $(\theta_{L1}, \theta_{L2})$ pair in the state space map once per pair. To test both pull directions (forward and backward), we change the leg orientations while keeping the pull direction of the robotic arm the same with respect to the tank. The tank is filled with uniform, spherical 0.8 mm glass beads, with a volume of 40 cm $\times$ 20 cm $\times$ 24 cm.

We compare these robot-arm pull test experiments to simulated estimations under the same conditions. We predicted the trajectory $([x, z, \theta_B]_t)$ of the legged robot by integrating the motion twist estimations $([v_x, v_z, \omega_y]_t)$ over small time increments (Δt) using the Euler method. The $[x, z, \theta_B]_0$ is the measured initial pose of the legged robot and the Δt is set as a time increment that results in small translational displacement, i.e., $||(\Delta x, \Delta z)||_2 \approx 1$ mm. The trajectory simulation terminates when the base plate hits the granular media or when any pull wrench can not satisfy the quasi-static assumption.

V. Results

Fig. 8 shows the measured motion and force trends of four different leg and load configurations (solid lines) in comparison to the simulated predictions (dashed and dotted lines). Overall, the simulations match the experimental amplitudes and trends measured in the glass bead media test. For these $(\theta_{L1}, \theta_{L2})$ pairs, different pullout forces and motions result depending on the pull direction (forwards or backwards). For pullout forces, both experiment and simulation results show that force first peaks near the start of motion, then plateaus. One limitation in the force simulation is the initial pull prediction ($x \sim 0$ mm) where the simulation does not account for any compaction or surface mounding that may occur for deflections < 3 mm in the stationary-to-motion transition. Describing the motions observed, despite the horizontal pull, the point p moves downward because the net force couples result in a net moment, increasing θ_B. The largest error in model prediction occurs for

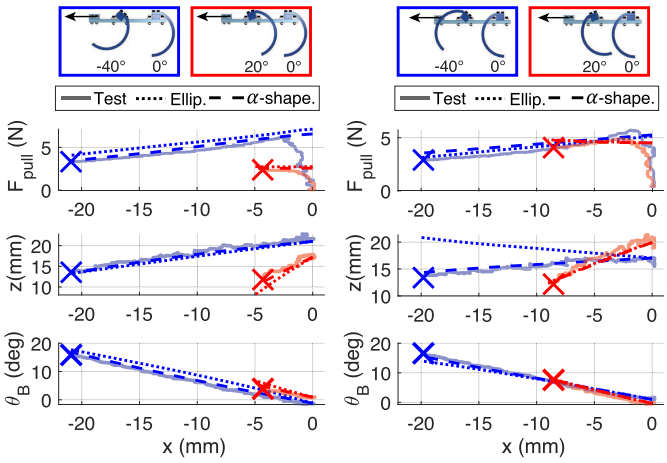

(a) Forward Pull (see Fig. 3a) (b) Backward Pull (see Fig. 3b)

Fig. 8. Comparison of predictions to the test measurements. String pull force of the slipping robot (row 1), and the trajectory of the point p (row 2) and body pitch angle θ_B (row 3) are compared for two different leg angle pairs (top legend). The marker X represents where the base plate of the robot hits the granular surface, and experiments are terminated.

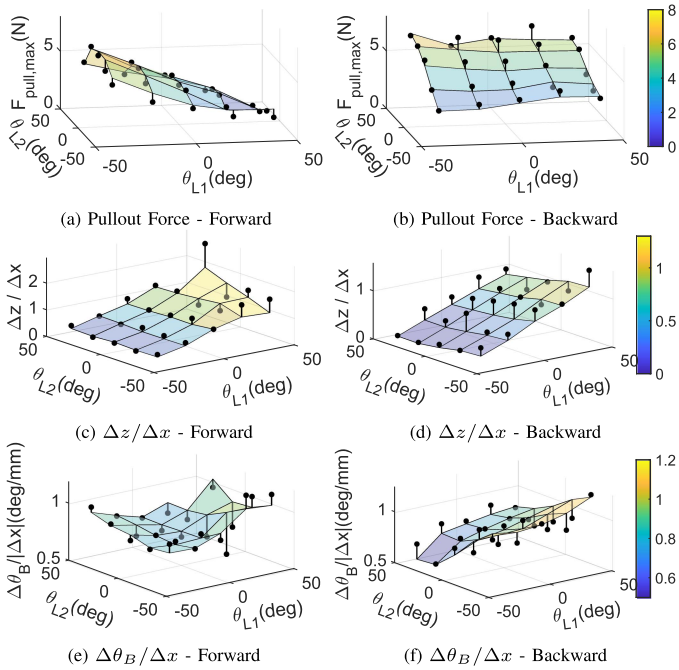

(a) Pullout Force - Forward (b) Pullout Force - Backward
(c) $\Delta z/\Delta x$ - Forward (d) $\Delta z/\Delta x$ - Backward
(e) $\Delta\theta_B/\Delta x$ - Forward (f) $\Delta\theta_B/\Delta x$ - Backward

Fig. 9. Comparison of alpha-shape method predictions to the test measurements in all tested leg angle pairs; (a, b) maximum horizontal pull force, (c, d) ratio of vertical to horizontal motion of winch point, p, (e, f) ratio of body rotation to the horizontal motion of p. Variable definitions are described in Fig. 3. The surface plots represent the simulation predictions and black dots are experimental measurements. Vertical lines represent the error between predictions and measurements. In the forward pull configuration, the data at $(\theta_{L1}, \theta_{L2}) = (40°, 40°)$ is absent because the RFT wrench can not resist the gravitational wrench.

the height estimate using the ellipsoid method in the backward pull direction for $(\theta_{L1}, \theta_{L2}) = (-40°, 0°)$, i.e. Fig. 8(b)-z (blue), probably due to ignoring the power dissipation of adjacent media (Section III-D). The alpha-shape method is therefore recommended for more consistent accuracy across different conditions.

Fig. 9 summarizes these results across the full set of $(\theta_{L1}, \theta_{L2})$ combinations tested, visualizing experiments and the alpha-shape simulations only. Fig. 9(a) and (b) show the pullout forces across different leg angle pairs. The forward pulls show the saddle shaped pullout forces, where the force increases with negative θ_{L1}. In contrast, the pullout forces in backward pulls increase with θ_{L2} while θ_{L1} has minor effects. In other words, the holding force in forward pulls relies more on the proximal legs, whereas in backward pulls the distal leg dominates the force.

The trajectories of winch point (p) in both pull directions share similar trends. Fig. 9(c) and (d) show the slope of the point trajectory in $\hat{x}$-$\hat{z}$ plane, or $\Delta z/\Delta x$. For both pull directions, the slope increases with θ_{L1} while θ_{L2} has minor effects. This implies that if the proximal leg increases θ_{L1} and contacts the ground further from point p, then the proximal legs experience low lift forces, easily sinking point p into the granular media. However, the rapid fall of the point p does not necessarily result in low pullout forces, as shown in the backward pull cases, e.g., $(\theta_{L1}, \theta_{L2}) = (40°, 40°)$. The relative change of the body orientation, or $\Delta\theta_B/\Delta x$ depicted in Fig. 9(e) and (f), shows a negative correlation with pullout forces in backward pull cases; there is not a strong trend in the forward pulling direction.

Table I summarizes the absolute errors in prediction of the two proposed simulation methods provide across the full set of experiments tested. The alpha-shape method results in 37% less error in force and trajectory predictions than the ellipsoidal method; however, the differences are not statistically significant in this case study. If precision is not critical in a particular application, the ellipsoidal method with simpler representation may be used.

TABLE I
ABSOLUTE ERRORS IN PREDICTIONS (MEAN ± STANDARD DEVIATION) IN ALL FORWARD AND BACKWARD PULLS

	Ellips.	α-shape
$F_{pull,\max}$ (N)	0.63 ± 0.42	$\mathbf{0.38 \pm 0.30}$
$\Delta z/\Delta x$	0.24 ± 0.19	$\mathbf{0.17 \pm 0.17}$
$\Delta\theta_B/\lvert\Delta x\rvert$ (°/mm)	0.14 ± 0.11	$\mathbf{0.08 \pm 0.07}$

VI. Robotic Tugging Demonstrations

As a demonstration of this modeling method for the analysis of legged tugging in granular media, we show how the robot can utilize RFT-GLS predictions to choose effective and energy-efficient leg anchor configurations for given pull loads. To meet a specific required tugging load capacity, the robot should burrow its legs to a leg angle pair and burrowing depth as prescribed by the results shown in Fig. 9. For a given leg angle pair, burrowing deeper increases tugging capacity, but also requires higher motor torques and more energy to execute. In this section, we evaluate the trade-off between input energy and anchor load capacity for a few example burrowing control cases with the MiniRQuad. This demonstration is intended only to test whether the controlled laboratory modeling results can inform more unconstrained, continuous walk-burrow-tugging on real sand.

TABLE II
CONTROL INPUTS AND THE RESULTANT BODY POSES OF THREE DIFFERENT LEG CONFIGURATIONS: DEEP-HIGH-LOAD-CAPACITY (DH), DEEP-LOW-LOAD-CAPACITY (DL), AND SHALLOW-HIGH-LOAD-CAPACITY (SH)

	DH	DL	SH
Retracting (θ_{L1},θ_{L2})	(-75°, -50°)	(-75°, -50°)	(-40°, -20°)
Final (θ_{L1},θ_{L2})	(-40°, 30°)	(-40°, 0°)	(-40°, 30°)
θ_B (°)	5.0 ± 0.4	8.9 ± 0.7	2.4 ± 0.7
$h\,(mm)$	34 ± 1	36 ± 2	47 ± 2
	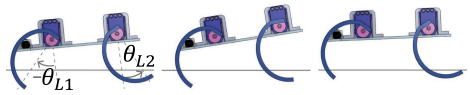		

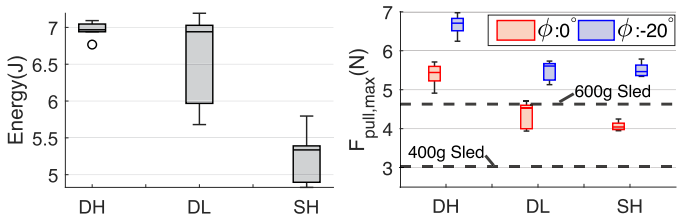

(a) Anchoring Energy (b) Predicted tug load capacity

Fig. 10. (a) Measured input energy during the anchoring process and (b) prediction of tug load capacities of each anchor mode. ϕ, as in Fig. 3, indicates either a horizontal (0°) or slight downward (−20°) pull direction.

A. MiniRQuad Test Setup

For tests, as shown in Fig. 1, we built a quadruped robot named MiniRQuad that uses four motors and is based off the control system of the MiniRHex [17]. MiniRQuad weighs 296 g and uses the same C-legs in Section IV with a longer wheelbase of 90 mm. We found that the trends in load capacity prediction of MiniRQuad remain the same as in the prototype tests (Fig. 9). We placed a current sensor (INA219 breakout, Adafruit) to monitor the power consumption of the leg motors and the microcontroller. The MiniRQuad is primarily designed to walk forward in granular media, so a winch motor (Micro metal gearmotor, Pololu) is placed on the back of the robot and incurs backward pulls when tugging. We test this robot on a loose media with a more realistic particle distribution: M90 regolith simulant [45] (#90 Silver Sand, P.W. Gillibrand, particle size ∼0.2 mm). The media volume is 180 cm × 90 cm × 20 cm. When computing RFT-GLS, we used 3D RFT model presented in [41] that requires only two tunable parameters to match media behavior. MiniRQuad is not optimally designed yet serves as a case study for further model demonstration.

B. Anchoring by Burrowing

We test three leg configurations to test as described in Table II: Deep High-load-capacity (DH), Deep Low-load-capacity (DL), and Shallow High-load-capacity (SH). For θ_{L2}, we set two angles, 30° and 0°, that show a high and a medium levels of load capacity as shown in Fig. 9(b). We chose θ_{L1} of −40° that minimizes leg travel after burrowing. We arbitrarily chose the two depths within the achievable range. The initial "retracting" pose represents the first phase of burrowing as in Fig. 2(b), while the "final" pose is the anchored state for tugging Fig. 2(c); Fig. 2 depicts the DH case. The mean and standard deviation of the final body angle and depth are reported over 6 trials under each condition. Note that the final depth, h_w, is influenced not only by the "final" leg pose, but also by the initial "retracting" pose. Because of the higher density of M90 and motor torque limitations, the legs are constrained to shallower depths than those tested in Section V.

Fig. 10(a) shows a significant energy consumption difference between the deep anchors (DH, DL) and the shallow anchor (SH). This measurement is performed for 8 seconds, and the idle power consumption is removed to isolate the effect of burrowing. On average, the DH and DL show 1.32 and 1.26 times greater energy consumption than SH, respectively. Each burrowing trial resulted in a θ_B and h_w combination, which we measure and use to predict the maximum pullout force of the burrowed robot, shown in Fig. 10(b), using the alpha-shape defined RFT-GLS. We use RFT-GLS displacement predictions when estimating peak tugging capacity because the maximum pullout force sometimes occurs after robot movement is induced by tugging.

We simulate two conditions to understand how anchor effectiveness changes over the trajectory of the payload: (1) the payload is far away and the tether is horizontal ($\phi = 0°$) and (2) the payload approaches the winch and the tether is directed downward ($\phi = -20°$). Anchor strength increases as the payload gets closer to the robot on flat terrain. The dashed horizontal lines represent the forces required to tug the 400 g sled and 600 g sled, as averaged over three pulling trials. The DH anchor mode results in the greatest load capacity, and is able to tug the 600 g payload in both ϕ conditions. However, the SH anchor requires less energy to perform and provides sufficient tugging capacity for pulling the 400 g sled. RFT-GLS enables the assessment of anchor load capacity sufficiency, taking into account estimated motions of the payload and robot during tugging.

C. Cyclical Walk-Burrow-Tugging

Here, we demonstrate energy and force trade-offs and the importance of selecting the appropriate anchor mode in a cyclical walk-burrow-tugging motion. We control the MiniRQuad to walk in a hard-coded ambling gait for 8 seconds, anchor via burrowing for 8 seconds, and then tug a sled loaded with either 400 g or 600 g as shown in Fig. 11. The tugging is controlled by tele-operation until the sled is a couple centimeters away from the winch. The MiniRQuad then un-burrows itself by performing a new walk sequence.

The energy consumption is recorded during the active walking and anchoring periods. The tug period length varies depending on the initial string length, so only the energy consumed during the last 8 seconds of the tug is counted in order to maintain comparable test conditions. Over the course of three repeated walk-burrow-tug cycles, as shown in Fig. 12, the MiniRQuad moves almost 1 m. In (a), the 400 g sled case, all three anchoring modes (DH, DL, SH) can successfully pull the sled, although the DH mode consumes 1.3 times greater energy than the SH mode. SH is the preferred anchoring option to reduce energy consumption. In (b), the 600 g sled case, only the DH mode successfully pulls the sled for all three cycles, as expected in the load capacity prediction shown in Fig. 10(b). SH and DL modes fail as marked with 'X' and consume comparable energy

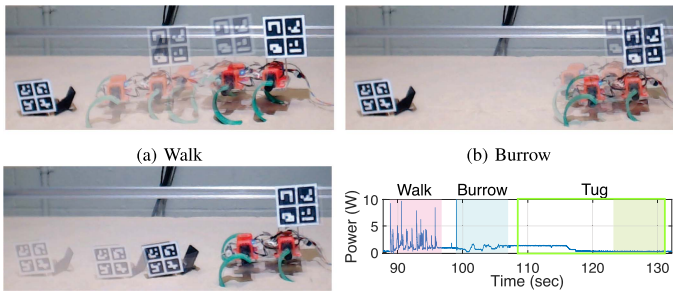

(a) Walk (b) Burrow (c) Tug (d) Power consumption

Fig. 11. MiniRQuad walk-burrow-tugging test. (a) MiniRQuad walks in amble gait for 8 seconds and then (b) anchors its legs for 8 seconds. (c) Finally, the winch motor tugs a sled loaded with test weights. (d) Power consumption of each stage of the control sequence. Because the tug time varies depending on the initial string length, only the last 8 seconds of the tug are considered for computing the consumed energy.

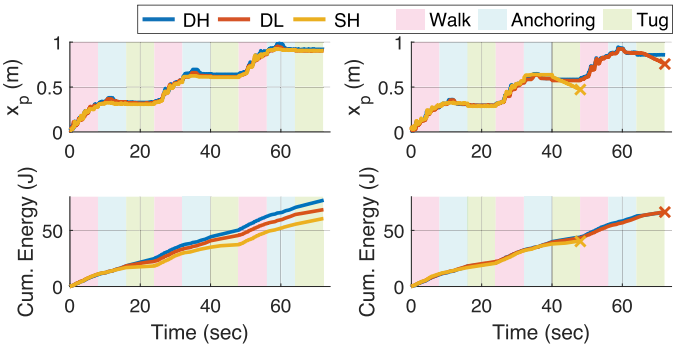

(a) 400g load (b) 600g load

Fig. 12. Cumulated energy consumption for 3 cycles of walk-burrow-tug control for two different sled weights. The top plots show that the resultant forward distances of the MiniRQuad robot measured by the ArUco marker are approximately 1 m. 'X' markers indicate the anchor failures.

to DH to maintain leg angles during tugging. DH is the preferred anchoring option to increase tugging force.

VII. Discussion

These experiments and demonstrations show the potential of simple, small, legged robots to perform forceful tugging on loose granular media by burrowing and anchoring their legs, augmenting their existing locomotion abilities. They also show that the RFT-GLS method provides force and motion predictions relevant to decision-making while burrowing and tugging. This study is performed at relatively shallow depths with small displacements and forces of a single robot not specifically designed for tugging. For future work, deeper burrowing can be studied for greater load capacity without specialized auxiliary anchor mechanisms. As our limit surface method employs 3D RFT, it operates under the same assumptions and limitations, namely that it may not work well for objects with sharp edges, and it does not account for localized jamming or fluidization of the granular media or surface topography. Additionally, the GLS assumes each wrench is generated from a unique twist. This unique pair assumption fails when the motion of an anchor predominantly slips in the granular media rather than breaking through the adjacent granules, e.g., a thin plate moving along

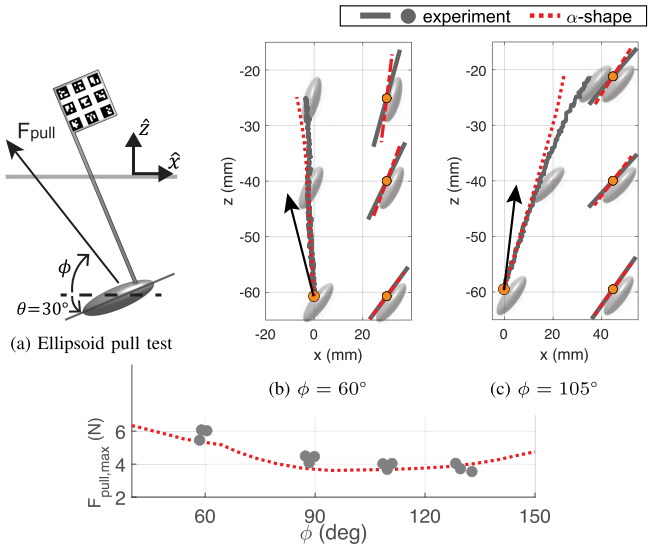

(a) Ellipsoid pull test (b) $\phi = 60°$ (c) $\phi = 105°$ (d) Pull test at $z = -7$cm

Fig. 13. Ellipsoid pull tests. (a) a 3D printed ellipsoid is placed at 7 cm depth with 30° body angle and a robot arm (UR10) pulls it out, maintaining the tension angle ϕ. (b, c) Comparison of predicted trajectories to the experimentally tracked trajectories. In each plot, the left shows the translational trajectory of the tether point, and the right shows the orientation of the anchor. The overlay images of the anchor, not to scale, show the experimentally tracked orientations. (c) Comparison between predicted and tested load capacities.

its tangent. RFT-GLS works best when these circumstances are uncommon.

A. Computational Efficiency

By utilizing the empirical RFT models, RFT-GLS is more computationally efficient than other existing methods, such as DEM which may take hours or even days to compute. As a benchmark for RFT-GLS, AMD Ryzen7 3700X CPU computes the point cloud in Fig. 4 in 0.8 seconds. The computation time of RFT-GLS is linearly proportional to both the number of sampled twists and the number of facets in the imported CAD mesh. Resolution in either the limit surface point cloud density or the solid body mesh can be reduced to speed up computation at the cost of wrench prediction accuracy. Alternatively, a pre-computed state space map can be used as described in Section III-E and computes the load capacity in 0.02 seconds. The state space map is especially useful in cases where real-time motion and load capacity predictions are desired. For comparison, DEM takes roughly 6 minutes to simulate 1 s of a single load case in one million particles, using Nvidia A100 GPU [46].

B. Application to Other Anchor Designs

One benefit of the RFT-GLS method is that these simulations required no *a priori* experiments with the real leg geometry. This is evidence that the RFT-GLS method is easily adaptable to new robot geometries. Functionally, RFT-GLS can be quickly applied to other geometries by inputting a new STL file and re-computing the RFT-GLS. For example, Fig. 13 shows the results, both experimental and simulated, for a generic shape. The ellipsoidal body is initialized at 7 cm depth and 30° body angle, then pulled upward with a constant F_{pull} direction, ϕ,

using the robot arm. Motion and force are tracked using the same methods as in Section IV. RFT-GLS once again provides reasonable estimates without special model tuning. Future work will explore the potential utility of this rapid granular interaction modeling method for the geometric design and control optimization of alternative robotic anchoring structures, including both legs and mechanisms other than legs.

REFERENCES

[1] A. E. Hosoi and D. I. Goldman, "Beneath our feet: Strategies for locomotion in granular media," *Annu. Rev. Fluid Mech.*, vol. 47, pp. 431–453, 2015.

[2] D. I. Goldman, "Colloquium: Biophysical principles of undulatory self-propulsion in granular media," *Rev. Modern Phys.*, vol. 86, no. 3, pp. 943–958, 2014.

[3] A. Thoesen and H. Marvi, "Planetary surface mobility and exploration: A review," *Curr. Robot. Rep.*, vol. 2, no. 3, pp. 239–249, 2021.

[4] J. Fernandez and A. Mazumdar, "Tail-based anchoring on granular media for transporting heavy payloads," *IEEE Robot. Automat. Lett.*, vol. 6, no. 2, pp. 1232–1239, Apr. 2021.

[5] C. Creager, K. Johnson, M. Plant, S. Moreland, and K. Skonieczny, "Push–pull locomotion for vehicle extrication," *J. Terramechanics*, vol. 57, pp. 71–80, 2015.

[6] H. Wei et al., "Review on bioinspired planetary regolith-burrowing robots," *Space Sci. Rev.*, vol. 217, no. 8, pp. 1–39, 2021.

[7] R. A. Russell, "Crabot: A biomimetic burrowing robot designed for underground chemical source location," *Adv. Robot.*, vol. 25, no. 1-2, pp. 119–134, 2011.

[8] L. K. Treers, B. McInroe, R. Full, and H. S. Stuart, "Mole crab-inspired verticalself-burrowing," *Front. Robot. AI*, pp. 1–17.

[9] A. Winter et al., "Razor clam to roboclam: Burrowing drag reduction mechanisms and their robotic adaptation," *Bioinspiration Biomimetric*, vol. 9, no. 3, 2014, Art. no. 036009.

[10] J. J. Tao, S. Huang, and Y. Tang, "Sbor: A minimalistic soft self-burrowing-out robot inspired by razor clams," *Bioinspiration Biomimetric*, vol. 15, no. 5, 2020, Art. no. 055003.

[11] A. A. Calderón, J. C. Ugalde, J. C. Zagal, and N. O. Pérez-Arancibia, "Design, fabrication and control of a multi-material-multi-actuator soft robot inspired by burrowing worms," in *Proc. IEEE Int. Conf. Robot. Biomimetics*, 2016, pp. 31–38.

[12] E. Del Dottore, A. Mondini, A. Sadeghi, V. Mattoli, and B. Mazzolai, "An efficient soil penetration strategy for explorative robots inspired by plant root circumnutation movements," *Bioinspiration Biomimetics*, vol. 13, no. 1, 2017, Art. no. 015003.

[13] N. D. Naclerio et al., "Controlling subterranean forces enables a fast, steerable, burrowing soft robot," *Sci. Robot.*, vol. 6, no. 55, 2021, Art. no. eabe2922.

[14] D. L. Christensen, S. A. Suresh, K. Hahm, and M. R. Cutkosky, "Let's all pull together: Principles for sharing large loads in microrobot teams," *IEEE Robot. Automat. Lett.*, vol. 1, no. 2, pp. 1089–1096, Jul. 2016.

[15] M. A. Estrada, S. Mintchev, D. L. Christensen, M. R. Cutkosky, and D. Floreano, "Forceful manipulation with micro air vehicles," *Sci. Robot.*, vol. 3, no. 23, 2018, Art. no. eaau6903.

[16] M. T. Pope et al., "A multimodal robot for perching and climbing on vertical outdoor surfaces," *IEEE Trans. Robot.*, vol. 33, no. 1, pp. 38–48, Feb. 2017.

[17] M. Barragan, N. Flowers, and A. M. Johnson, "MiniRHex: A small, open-source, fully programmable walking hexapod," in *Proc. Robot.: Sci. Syst. Workshop "Design Control Small Legged Robots*," 2018.

[18] C. Li, T. Zhang, and D. I. Goldman, "A terradynamics of legged locomotion on granular media," *Science*, vol. 339, no. 6126, pp. 1408–1412, 2013.

[19] T. Zhang and D. I. Goldman, "The effectiveness of resistive force theory in granular locomotion," *Phys. Fluids*, vol. 26, no. 10, 2014, Art. no. 101308.

[20] D. Li, S. Huang, Y. Tang, H. Marvi, J. Tao, and D. M. Aukes, "Compliant fins for locomotion in granular media," *IEEE Robot. Automat. Lett.*, vol. 6, no. 3, pp. 5984–5991, Jul. 2021.

[21] S. Agarwal et al., "Modeling of the interaction of rigid wheels with dry granular media," *J. Terramechanics*, vol. 85, pp. 1–14, 2019.

[22] S. Agarwal, A. Karsai, D. I. Goldman, and K. Kamrin, "Surprising simplicity in the modeling of dynamic granular intrusion," *Sci. Adv.*, vol. 7, no. 17, 2021, Art. no. eabe0631.

[23] C. Cao, C. Creager, D. K. Lieu, and H. S. Stuart, "Mobility experiments assessing performance of front-back differential drive velocity on sandy terrain," in *Proc. Int. Soc. Terrain-Veh. Syst.*, 2021, pp. 1–9.

[24] G. Meyerhof and J. Adams, "The ultimate uplift capacity of foundations," *Can. Geotech. J.*, vol. 5, no. 4, pp. 225–244, 1968.

[25] D. White, C. Cheuk, and M. Bolton, "The uplift resistance of pipes and plate anchors buried in sand," *Géotechnique*, vol. 58, no. 10, pp. 771–779, 2008.

[26] A. S. Vesić, "Breakout resistance of objects embedded in ocean bottom," *J. Soil Mechanics Found. Division*, vol. 97, no. 9, pp. 1183–1205, 1971.

[27] R. Merifield and S. Sloan, "The ultimate pullout capacity of anchors in frictional soils," *Can. Geotech. J.*, vol. 43, no. 8, pp. 852–868, 2006.

[28] K. F. Lee, J. F. Davidson, J. Akroyd, and M. Kraft, "Lifting a buried object: Reverse hopper theory," *Chem. Eng. Sci.*, vol. 105, pp. 198–207, 2014.

[29] B. M. Das and S. K. Shukla, *Earth Anchors*. Plantation, FL, USA: J. Ross Pub, 2013.

[30] R. Rowe and E. Davis, "The behaviour of anchor plates in sand," *Geotechnique*, vol. 32, no. 1, pp. 25–41, 1982.

[31] H.-H. Zhu et al., "Experimental and numerical investigation of uplift behavior of umbrella-shaped ground anchor," *Geomech. Eng*, vol. 7, no. 2, pp. 165–181, 2014.

[32] S. Athani, P. Kharel, D. Airey, and P. Rognon, "Grain-size effect on uplift capacity of plate anchors in coarse granular soils," *Geotechnique Lett.*, vol. 7, no. 2, pp. 167–173, 2017.

[33] T. M. Evans and N. Zhang, "Three-dimensional simulations of plate anchor pullout in granular materials," *Int. J. Geomechanics*, vol. 19, no. 4, 2019, Art. no. 4019004.

[34] S. Goyal, A. Ruina, and J. Papadopoulos, "Planar sliding with dry friction Part 1. limit surface and moment function," *Wear*, vol. 143, no. 2, pp. 307–330, Mar. 1991.

[35] R. D. Howe and M. R. Cutkosky, "Practical force-motion models for sliding manipulation," *Int. J. Robot. Res.*, vol. 15, no. 6, pp. 557–572, 1996.

[36] N. Chavan-Dafle, R. Holladay, and A. Rodriguez, "Planar in-hand manipulation via motion cones," *Int. J. Robot. Res.*, vol. 39, no. 2-3, pp. 163–182, 2020.

[37] J. Shi, J. Z. Woodruff, P. B. Umbanhowar, and K. M. Lynch, "Dynamic in-hand sliding manipulation," *IEEE Trans. Robot.*, vol. 33, no. 4, pp. 778–795, Aug. 2017.

[38] Y. Zhu, L. Abdulmajeid, and K. Hauser, "A data-driven approach for fast simulation of robot locomotion on granular media," in *Proc. IEEE Int. Conf. Robot. Automat.*, 2019, pp. 7653–7659.

[39] J. Gray and G. Hancock, "The propulsion of sea-urchin spermatozoa," *J. Exp. Biol.*, vol. 32, no. 4, pp. 802–814, 1955.

[40] L. K. Treers, C. Cao, and H. S. Stuart, "Granular resistive force theory implementation for three-dimensional trajectories," *IEEE Robot. Automat. Lett.*, vol. 6, no. 2, pp. 1887–1894, Apr. 2021.

[41] S. Agarwal, D. I. Goldman, and K. Kamrin, "Real-time modeling of three-dimensional granular intrusion," 2022, *arXiv:2205.14920*.

[42] N. Gravish, P. B. Umbanhowar, and D. I. Goldman, "Force and flow at the onset of drag in plowed granular media," *Phys. Rev. E*, vol. 89, no. 4, 2014, Art. no. 42202.

[43] H. Edelsbrunner and E. P. Mücke, "Three-dimensional alpha shapes," *ACM Trans. Graph.*, vol. 13, no. 1, pp. 43–72, 1994.

[44] K. Hormann, "Barycentric interpolation," in *Approximation Theory XIV: San Antonio 2013*. Berlin, Germany: Springer, 2014, pp. 197–218.

[45] H. A. Oravec, V. M. Asnani, C. M. Creage, and S. J. Moreland, "Geotechnical review of existing Mars soil simulants for surface mobility," in *Proc. Earth Space*, 2021, pp. 157–170.

[46] L. Fang, R. Zhang, C. V. Heuvel, R. Serban, and D. Negrut, "Chrono:: GPU: An open-source simulation package for granular dynamics using the discrete element method," *Processes*, vol. 9, no. 10, 2021, Art. no. 1813.